

AD-A084 757

AIR FORCE GEOPHYSICS LAB HANSCOM AFB MA
DEVELOPMENT OF TECHNIQUES TO SPECIFY CLOUDINESS AND RAINFALL RA--ETC(U)
OCT 79 H S MUECH, T J KEZGAN
AFGL-TR-79-0255

ML

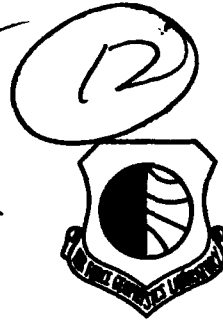
UNCLASSIFIED

AD
A084757

END
DATE
FILMED
6-80
DTIC

ADA 084757

~~LEVEL~~



AFGL-TR-79-0255
ENVIRONMENTAL RESEARCH PAPERS, NO. 981

Development of Techniques to Specify Cloudiness and Rainfall Rate Using GOES Imagery Data

H. STUART MUENCH
THOMAS J. KEEGAN

26 October 1979

DTIC
ELECTE
MAY 28 1980
S D A

Approved for public release; distribution unlimited.

FILE COPY

ATMOSPHERIC DIVISION PROJECT 6479
AIR FORCE GEOPHYSICS LABORATORY

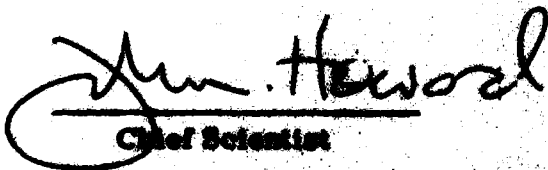
RESEARCH AND DEVELOPMENT DIVISION

AIR FORCE GEOPHYSICS LABORATORY

This report has been reviewed by the ESD Information Office (OI) and is releasable to the National Technical Information Service (NTIS).

This technical report has been reviewed and is approved for publication.

FOR THE COMMANDER


Chief Scientist

Qualified requesters may obtain additional copies from the Defense Documentation Center. All others should apply to the National Technical Information Service.

Unclassified

SECURITY CLASSIFICATION OF THIS PAGE (When Data Entered)

REPORT DOCUMENTATION PAGE		READ INSTRUCTIONS BEFORE COMPLETING FORM
1. REPORT NUMBER AFGL-TR-79-0255	2. GOVT ACCESSION NO. AID-A084757	3. SPECIFIC CATALOG NUMBER
4. TITLE (and Subtitle) DEVELOPMENT OF TECHNIQUES TO SPECIFY CLOUDINESS AND RAINFALL RATE USING GOES IMAGERY DATA	5. TYPE OF REPORT & PERIOD COVERED Scientific. Final.	
7. AUTHOR(s) H. Stuart/Muench Thomas J./Keegan	6. PERFORMING ORG. REPORT NUMBER ERP No. 681	
9. PERFORMING ORGANIZATION NAME AND ADDRESS Air Force Geophysics Laboratory (LYU) Hanscom AFB Massachusetts 01731	8. CONTRACT OR GRANT NUMBER(s)	
11. CONTROLLING OFFICE NAME AND ADDRESS Air Force Geophysics Laboratory (LYU) Hanscom AFB Massachusetts 01731	10. PROGRAM ELEMENT, PROJECT, TASK AREA & WORK UNIT NUMBERS 62101F 66700802 17.82	
14. MONITORING AGENCY NAME & ADDRESS (if different from Controlling Office) (15) +	12. REPORT DATE 26 Oct 1979	
	13. NUMBER OF PAGES 46	
	15. SECURITY CLASS. (of this report) Unclassified	
	15a. DECLASSIFICATION/DOWNGRADING SCHEDULE	
16. DISTRIBUTION STATEMENT (of this Report) Approved for public release; distribution unlimited.		
17. DISTRIBUTION STATEMENT (of the abstract entered in Block 20, if different from Report) (14) AFGL-TR-79-0255, AFGL-ERF-682		
18. SUPPLEMENTARY NOTES (9) Final repts		
19. KEY WORDS (Continue on reverse side if necessary and identify by block number) Satellite imagery Precipitation specification Meteorology Cloud specification GOES Cloud reflectance Objective forecasting Anisotropic scattering		
20. ABSTRACT (Continue on reverse side if necessary and identify by block number) This report summarizes the work accomplished during the first phase of an investigation concerning methods of introducing digitized satellite imagery into short-range, objective forecasting operations. The data archive being assembled for this study is described, with particular attention given to the steps taken to maximize the accuracy of the satellite imagery. These steps included fine tuning the navigation and selecting procedures for normalizing the data by correcting for the effects of Lambertian and anisotropic scattering.		

DD FORM 1 JAN 73 1473 EDITION OF 1 NOV 65 IS OBSOLETE

Unclassified

SECURITY CLASSIFICATION OF THIS PAGE (When Data Entered)

401372 xlv

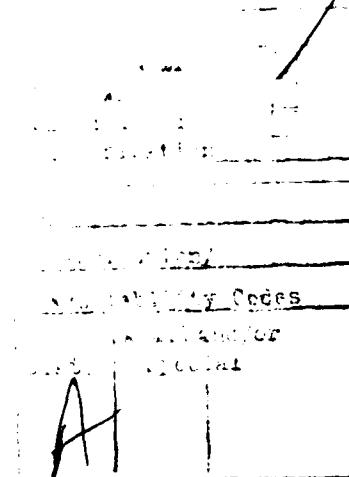
Unclassified

20. Abstract (Continued)

Consistency of the data, spatial and temporal, was tested by analysis of ground reflectance during cloudless days, and a pilot test of the specification of single layers of clouds was conducted. Both of these tests gave encouraging results. An investigation of specifying precipitation rate, using just the visible reflectance and infrared temperature of the cloud top, also produced good results. Nomograms for the average rate during the hour following the satellite observation, as well as for the probability of observing more than 0.01 in. and 0.10 in. of precipitation, are illustrated. Two appendices present the geometrical and optical equations relevant to the investigation.

Unclassified

SECRETARY OF DEFENSE, WASHINGTON, D. C. 20301-6000



Contents

1. INTRODUCTION	7
2. GOES DATA ARCHIVE	8
2.1 Data Collection	8
2.2 Positioning Satellite Data	9
2.3 Normalizing GOES Visible Imagery Data	13
3. BRIGHTNESS ANALYSIS	19
3.1 Ground Brightness	19
3.2 Local Variations in Ground Reflectance	20
3.3 Time Variations in Ground Reflectivity	22
3.4 Time Variations in Cloud Reflectivity	23
4. ESTIMATION OF RAINFALL RATE USING GEOSYNCHRONOUS SATELLITE IMAGERY DATA	23
4.1 Rainfall Rate and Sky Brightness	26
4.2 Surface Visibility and Sky Brightness	27
4.3 Specification of Rainfall from Satellite Imagery Data	29
4.4 Data Extraction and Processing	31
4.5 Results	32
4.6 Potential Specification Improvements	34
5. CONCLUSIONS	34
REFERENCES	37
LIST OF SYMBOLS	39
APPENDIX A: Basic Equations and Satellite-Solar Geometry	41
APPENDIX B: Algorithm for Normalizing GOES Video Values	45

Illustrations

1. Area Covered by Archived Satellite Images and Location of Associated Meteorological Data	10
2. Atmospheric Reflection at 0.55 to 0.75μ as a Function of Solar Zenith Angle for Four Cloud Models, and Lines Depicting $f(\xi)$	16
3. Anisotropic Scattering Function for Bright Clouds, Based on Surface Radiation Data at Otis AFB, Massachusetts, and GOES Video Data	18
4. Anisotropic Scattering Function for Bright Clouds, Based on Surface Radiation Data at Burlington, Vermont, and GOES Video Data	18
5. Geometric Arrangement of Grids Used in Computing Statistics from Video Imagery Data in Vicinity of Test Stations	20
6. Monthly Variation of Average Brightness (Video Count, 0-255) as a Function of Solar Elevation Angle	23
7. Clear-sky Reflectance of the Ground at Four Locations (Bedford, Massachusetts, Pittsburgh, Pennsylvania, Dulles International Airport, Virginia, and Albany, New York) as a Function of Month	23
8. Reflectance Sensed by GOES under Conditions of: (a) Clear skies, low scattered clouds, and low broken clouds; (b) high broken clouds and high overcast clouds, as a function of month	24
9. Probability of 5 min Precipitation Rate Versus Cloud Reflectivity, for \geq trace, for ≥ 0.03 in. (0.8 mm), for ≥ 0.10 in. (2.5 mm), for ≥ 0.30 in. (1.6 mm) and for ≥ 1.00 in. (25.4 mm) per hour	28
10. Effect of Haze on Total Radiation at the Surface, in mid-April 1977, at Otis AFB, Massachusetts	28
11. One-hour Rainfall as a Function of Normalized Cloud Reflectivity and Infrared Cloud Temperature	33
12. Probability of One-hour Rainfall ≥ 0.01 in. (0.25 mm) as a Function of Normalized Cloud Reflectivity and Infrared Cloud Temperature	33
13. Probability of One-hour Rainfall ≥ 0.10 in. (2.54 mm) as a Function of Normalized Cloud Reflectivity and Infrared Cloud Temperature	33
A1. Illustration of Parameters Describing Position of Satellite Relative to Position on Earth	43
A2. Illustration of Angles Describing Direction of Sun and Direction of Satellite Relative to Position on Earth	44
B1. Normalized Cloud Reflectivity as a Function of Video Count and Time of Day, for 16 Apr, 42N and 74W, with Calibration Count (C_0) Equal to 60	46

Tables

1. GOES Images Archived by Months	12
2. Reflectance Statistics for Clear Days in Vicinity of Bedford, Massachusetts, at 1600 UT, as a Function of Area, on 29 April; 3, 12, and 23 May 1977	21
3. Reflectance Statistics Over 9×9 Pixel Areas Surrounding Bedford, Massachusetts, at 1600 UT, for Selected Clear Days in 1977	22

Development of Techniques to Specify Cloudiness and Rainfall Rate Using GOES Imagery Data

1. INTRODUCTION

One of the main problems facing Air Weather Service is the need to automate as many of the functions as possible and, at the same time, improve the effectiveness. The specification and short-range forecasting of cloud conditions and precipitation, a field in which weather satellite information has become increasingly useful, are involved in many of these functions. In recent years, the satellites have been transmitting digital values instead of analog signals, and while the data rates are very high, the numbers can be processed automatically by computer to produce a wide variety of products to aid the forecaster and his customers. We can easily envision a complex, yet flexible, computer system that automatically produces forecasts for routine operations, but, at the same time, operates interactively with a forecaster for unusual conditions, or for special operations. Within such a system, specification and forecasting would be in probabilistic terms, enabling users to make cost effective decisions.

To realize such an ideal, we need a starting point. Experience with short-range forecasting has taught that the best starting point is a good observation. Thus, the first aim is to relate the satellite observations to operationally important weather parameters such as cloud cover, precipitation, and visibility. The

(Received for publication 25 October 1979)

relations sought are objective ones that can be easily computer programmed. In addition, the relations must contain information on accuracy, such as the probability of a variety of conditions, since weather sensitive operations require more than just the most probable condition.

This report is intended to answer questions about satellite data acquisition and processing, and to present results of techniques developed for the purpose of specifying cloud cover and rainfall rate, given GOES imagery information.

2. GOES DATA ARCHIVE

Before proceeding to develop objective, statistically-based techniques to specify and predict weather parameters, one must have a data base. The means for acquiring such a data base were present in the AFGL man-computer interactive data access system (McIDAS) package, in the form of a microprocessor controlled tape recorder system; namely, the offline data ingest system (ODIS), which can operate independently of the McIDAS computer, recording satellite images of several optional sizes and resolutions, and becoming the basis for a routine data archive.

2.1 Data Collection

The natural tendency of researchers with a data archive capability is to save all received data, whether or not there is foreseeable use for these data. However, with a very high information rate from satellites, this is not a practical method of operation (at least for our recording capability). Several real limitations were considered. The ODIS cannot operate rapidly enough to record both video channel data at 1/2-mi (0.9 km) resolution and 4-mi (7 km) IR channel data, simultaneously. Both channels can be recorded at coarser video resolution. The basic size unit for recording is one McIDAS TV frame consisting of 500 rows with 700 pixels (or elements) to a row, although larger arrays can be recorded. The tape recorder, with 9 tracks and 800 character-per-inch density, can record about 24 TV frames of video and corresponding IR on a 2400-ft reel. With two GOES within range of AFGL (East and West), each transmitting full disc images every half hour, there would be no difficulty filling many tapes every day, provided that we had sufficient tapes and storage, as well as the manpower for frequent changes. With limited resources, compromises were necessary.

The data requirements could well be met with a geographically fixed region, with the best resolution of video and IR data feasible, and recorded on a regular basis (to avoid sampling bias). The region chosen extends from Michigan to Nova Scotia and from Maine to North Carolina, with a wide variety of weather conditions

and with varying topography (see Figure 1). A 1-mi (1.8 km) resolution for video and 4-mi (7 km) resolution for IR were chosen, in order to provide maximum flexibility in data processing. Images were scheduled at hourly intervals, on the hour, to match the hourly airways weather observations which were to be used in technique development. The schedule was set for eight daylight hours each day, week days only. During periods of special interest, images were recorded at half-hourly intervals, and several series of night-time IR-only images have been recorded.

To supplement the GOES imagery data and provide further source material for technique development and verification, we have conventional weather data sources, including weather facsimile, airways teletype circuit, the military COMEDS circuit, and GOES facsimile. In addition, a high-speed weather teletype circuit is now linked directly to McIDAS, allowing the archiving of hourly weather reports on magnetic tape. Finally, we have microfiche copies of surface observations (MF-1-10A, 10B), as well as Local Climatological Data (for hourly rainfall), for stations shown in Figure 1 and radiosonde data (WBAN 33) for all stations in the area.

2.2 Positioning Satellite Data

The task of the meteorologist is considerably more difficult if he is uncertain of the geographical location of the weather data. When the location is uncertain, he finds it difficult in estimating pattern motion and arrival time. Some years ago, this was a common problem with reports from ships and aircraft, but modern electronics has greatly reduced such navigation errors. However, while ship and aircraft navigation problems have been largely solved, we now have the very challenging problem of navigating or finding the geographical position of weather satellite data. Certainly, it makes little sense to have data with 1/2-mi or 1-mi resolution to forecast weather systems 5 to 25 mi (9 to 45 km) in size, if the position uncertainty is of the order of 10 to 30 mi (18 to 54 km).

In the first decade of satellite meteorology, the principal data form was a black-and-white picture, with several uncalibrated shades of gray. At readout centers, computers used satellite orbital and attitude information to generate grids of latitude, longitude, and coastline, which were overlaid (electronically) upon the picture. The grids did not always fit the pictures perfectly and locating a point in the nonlinear coordinate system was not easy. Positioning errors of 20 to 40 miles (36 to 72 km) could occur. With the advent of the geosynchronous satellite, as well as the interactive computer systems, such as McIDAS, positioning data has been greatly facilitated. Basically, this is a problem in geometry, requiring the position of the satellite relative to the earth and also the direction in which the

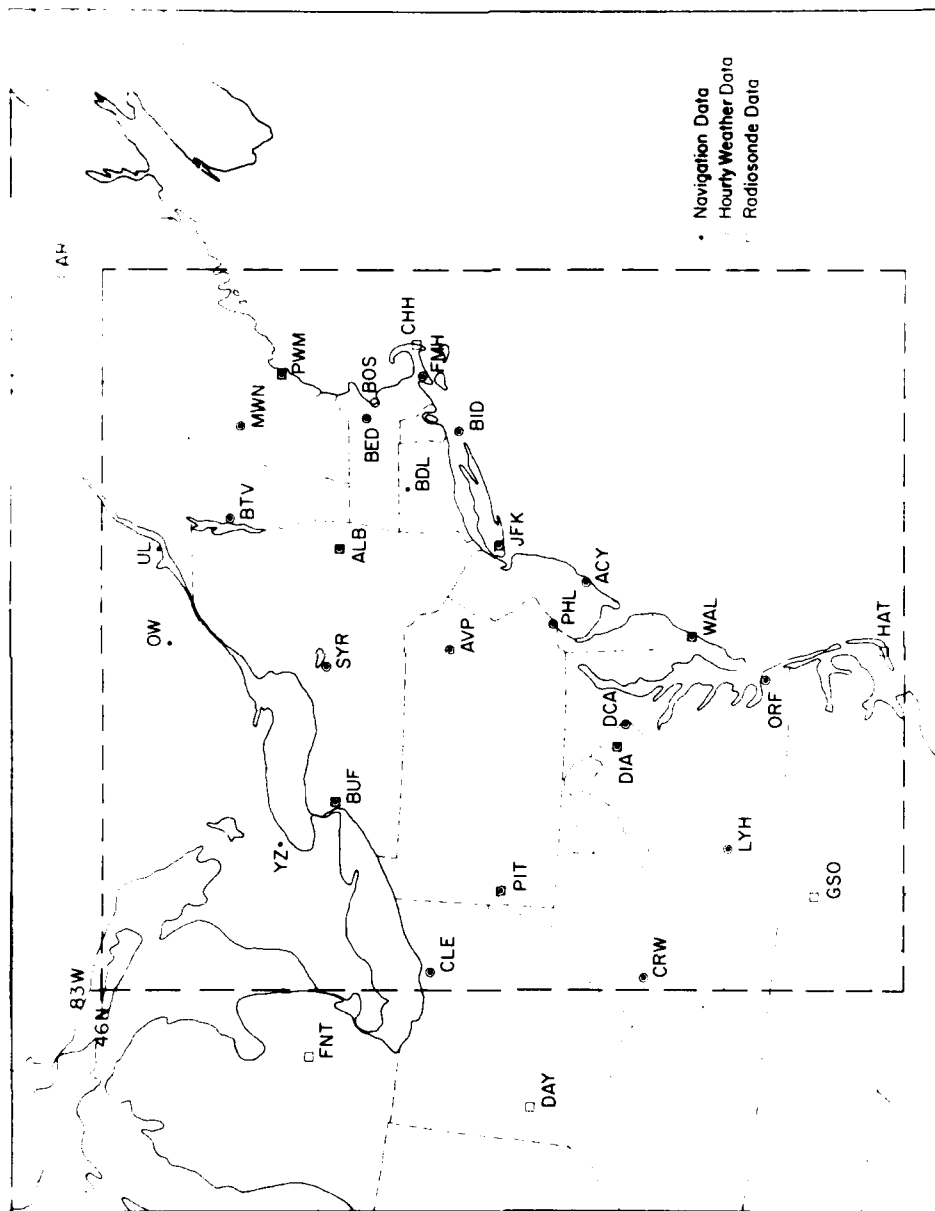


Figure 1. Area Covered by Archived Satellite Images and Location of Associated Meteorological Data

sensors are pointing. However, the position and particularly the pointing angles must be known very precisely at all times, because at geosynchronous orbits, a small error may cause great positional errors on the earth. Given about ten parameters (for example, orbit values, spin rate, axis orientation), the McIDAS can solve the geometry problem to give either, for example, longitude-latitude for any row and element of satellite data or the row and element for any latitude and longitude on the earth. For accurate navigation, one must have the best possible values for the satellite parameters, which can be accomplished through frequent updates of orbital parameters (using bulletins from the National Environmental and Satellite Service) and through a daily routine using the McIDAS. In this routine, 1/2-mile resolution images are displayed and known landmarks identified in a series of pictures; the computer determines parameters to produce optimum specification of position.

The original plan was to use simply the McIDAS navigation to forecast the satellite coordinates (row and element numbers) for the northwest corner of our standard archive image (46 N, 83 W) for each image of the day, and enter a list of times and coordinates into the ODIS about 0800 LT each day. These coordinates change from hour to hour as the satellite meanders in its position almost directly over the equator, and even the axis of rotation changes. Unfortunately, in this procedure we used the interactive navigation of the previous day to project the starting point coordinates 20 to 28 hours into the future. The largest errors were in the element number and on some images, the left and right edges were 100 to 200 km west of the planned locations. More recently, the McIDAS and the ODIS were modified such that the McIDAS is given the schedule about 0800 LT, but the computer transfers information on satellite coordinates based on recent navigation to ODIS, just prior to the start of each image.

To extract satellite video and IR values over selected weather stations for specification studies, there was a need for the satellite coordinates of the stations for each imaged archived. The McIDAS was used to produce listings of the coordinates for each station shown in Figure 1. However, in the process of the daily navigation update, the operator normally uses climatologically favored clear-weather targets near Baja, California, Venezuela, or Peru. This procedure results in some loss of accuracy at distances as far away as northeast United States, and errors in position of prominent landmarks were found to be as large as 5 to 15 nm (9 to 27 km). To reduce this error, a "fine-tuning" is done, using the archived data to find recognizable landmarks. The same row and element corrections are applied to all points in the image, even though spatially varying corrections might be a little more accurate (and more difficult to compute). Tests have shown that with up to 80 percent cloud cover, the final navigation with fine correction is good to about ± 2 to 4 nm (4 to 7 km). Some images are too completely filled

with clouds to obtain a fine correction. In such cases, one can either pass up the data, or use the McIDAS coordinates without fine correction. Alternatively, one may make an interpolation based on corrections for the previous and following days. While the interpolation may seem risky, the corrections often have remarkable day-to-day consistency, allowing the improved navigation for meteorologically important images that might otherwise be discarded.

Table 1 shows the number of hours of data that have been collected and also the number with the navigation "fine-tuned." Only the 1977 data, however, were available for the analyses reported herein.

Table 1. GOES Images Archived by Months

	1977		1978		1979	
	On Tape	Fine Navigation	On Tape	Fine Navigation	On Tape	Fine Navigation
Jan.	--	-	14	0	96	25
Feb.	38	30	50	10	109	0
Mar.	139	99	155	88	79	20
Apr.	107	107	140	101	137	89
May	120	120	163	145	150	109
June	104	94	142	120	150	110
July	97	94	38	37	*	*
Aug.	75	73	27	24	*	*
Sept.	56	50	12	12	*	*
Oct.	135	132	40	40		
Nov.	110	58	166	81		
Dec.	83	0	145	84		
Total	1064	857	1092	742	721	353
Total through June 1979						
On Tape 2877						
Fine Navigation 1952						

*Indicates tabulation is not complete

2.3 Normalizing GOES Visible Imagery Data

The GOES visible sensors respond to the radiance N received from objects within the field of view and within a spectral bandwidth of 0.5 to 0.75 microns. The information transmitted is a digital "count," 0 through 63, that is proportional to the square root of the radiance. Therefore, to compute radiance:

$$N = k C^2$$

where C is the count and k the proportionality constant. Naturally, radiance will vary as the illumination changes with varying solar elevation angle, and we should have a more conservative property to associate with clouds and terrestrial background. The obvious choice would be to compute the reflectance of the surface \tilde{r} ("albedo" for a limited spectral bandwidth) defined by*

$$\tilde{r} = \tilde{F}_c^* / (\tilde{H}^* \cos \xi) = \left(\int_0^\pi \tilde{N} d\Omega \right) / (\tilde{H}^* \cos \xi) \quad (1)$$

where \tilde{F}_c^* is the upward radiant flux due to the atmosphere; \tilde{H}^* the solar irradiance; and N the satellite measured radiance.

For a perfect diffuse reflector, $\tilde{r} = 1$ and $\tilde{N} = f(\Omega)$. We can define the radiance for an overhead sun by $\tilde{N}_0 = \tilde{H}^* \cos 0^\circ$ and the associated satellite video count would be C_0 (designed to be approximately 63). Using these relationships to substitute for \tilde{H}^* , we can compute reflectance by

$$\tilde{r} = \frac{\int_0^\pi \tilde{N} d\Omega}{\tilde{N}_0 \cos \xi} = \frac{1}{\pi} \int_0^\pi \left(\frac{C}{C_0} \right)^2 \frac{1}{\cos \xi} d\Omega \quad (2)$$

For a uniformly reflecting diffuse surface or "Lambertian" surface, we would have

$$\tilde{r} \text{ (Lambertian)} = \frac{1}{\cos \xi} \left(\frac{C}{C_0} \right)^2 \quad (3)$$

Unfortunately, most surfaces, and clouds in particular, are not uniform reflectors. Further, for a given cloud we get only one satellite measurement at a time and cannot integrate the radiance over the hemisphere. This means we

*See List of Symbols, page 39.

cannot obtain a conservative quantity by simply squaring C/C_0 and dividing by the cosine of the solar zenith angle.

Sikula and Vonder Haar¹ approached this problem by introducing the anisotropic scattering factor χ defined by

$$\chi = \tilde{r}/(\tilde{N}/\tilde{N}_0 \cos \xi) \quad (4)$$

which is the ratio of cloud reflectivity to the apparent reflectivity observed by the satellite. We can then compute cloud reflectivity \tilde{r}_c by

$$\tilde{r}_c = \chi \frac{\tilde{N}_c}{\tilde{N}_0 \cos \xi} = \chi \frac{1}{\cos \xi} \left(\frac{C}{C_0} \right)^2 \quad (5)$$

There is one more complication: For a given cloud, \tilde{r}_c is a function of the zenith angle of the sun, with the cloud being more reflective at large zenith angles than at small. We must thus normalize to a fixed solar zenith angle, preferably zero degrees or overhead sun. Sikula and Vonder Haar¹ found the normalized reflectivity

$$\tilde{r}_0 = \tilde{r} \text{ times } f(\xi)$$

and thus

$$\tilde{r}_0 = \chi f(\xi) \left[\frac{\tilde{N}}{\tilde{N}_0 \cos \xi} \right] = \chi f(\xi) \frac{1}{\cos \xi} \left(\frac{C}{C_0} \right)^2 \quad (6)$$

They then constructed tables of the factor χ for different types of surface (cloud, water, snow, forest) and different solar azimuth and zenith angles, as well as different satellite azimuth and zenith angles. The sources of material for their tables primarily were aircraft measurements of cloud scattering, using photometric devices. A single aircraft in a relatively short time can take a large number of observations of \tilde{N} for varying scattering angles and even compute reflectivity through a hemispheric integration. Unfortunately, the aircraft often do not stay aloft long enough for large changes in solar zenith angle, and when they do, there is a risk that significant changes in cloud structure may occur. As a result, it is very difficult to determine the $f(\xi)$ necessary to normalize to overhead sun.

1. Sikula, G.J., and Vonder Haar, J.H. (1972) Very Short Range Local Area Weather Forecasting Using Measurements from Geosynchronous Meteorological Satellites, AFCRL-72-0260, AD 744 098, Final Report, Contract F19628-71-C-0073.

Liou² made calculations of \bar{r} for several types of clouds using cloud models and rather lengthy Mie-scattering computer programs. While his calculations lacked some physical reality in excluding the ice clouds often found on top of deep cloud systems, at least he was able to treat the varying solar zenith angle in a complete and systematic fashion. Most of the data presented by Liou were for the complete solar spectrum (for example, \bar{r}), but by allowing for the lower absorption and higher transmission in the 0.55 to 0.75 micron band we have computed \tilde{r}_o as shown by the solid curves in Figure 2. Superimposed on this same figure are dashed lines representing $f(\xi)$ from Sikula and Vonder Haar,¹ which are quite different, particularly for the most reflective clouds. For this study, we chose to adopt the reflection values \tilde{r} based on Liou² as better representing the variation with zenith angle because the observational data of Sikula and Vonder Haar were not complete. An empirical relation that fits all but the cumulus cloud (Cu) is

$$\tilde{r}_o \approx \left[1.09 - \frac{2 \left\{ \left(1.09 - \frac{\chi}{\cos \xi} \right) \left(\frac{C}{C_o} \right)^2 \right\}}{1 + \cos^{1/2} \xi} \right] \quad (7)$$

When we started to use tables of χ from Sikula and Vonder Haar¹ to normalize GOES East data using Eq. (7), we encountered further problems. For a location such as New York, there were only 9 values of χ to cover all solar azimuth and zenith angles, making interpolation difficult. In addition, in preparing the tables, we noted that there were no observations between 25 and 45 degrees of solar zenith angle.³ Certainly, it was desirable to have more detailed information on χ , for better resolution. Fortunately, we can use ground-based radiometers together with satellite measurements to make estimates of χ . We define χ :

$$\chi \equiv \frac{\tilde{r}_c}{\tilde{N}_c / \tilde{N}_o \cos \xi} = \frac{\tilde{r}_c}{\tilde{N} / \tilde{N}_o \cos \xi - \tilde{N}_g / \tilde{N}_o \cos \xi} \quad (8)$$

In order to compute χ , we need \tilde{r}_c as well as satellite determined \tilde{N} . Therefore,

$$\tilde{r}_c = \tilde{F}_c^* / \tilde{N}^* \cos \xi = (\tilde{H}^* \cos \xi - \tilde{H}_g - A) / \tilde{H}^* \cos \xi \quad (9)$$

where \tilde{H}_g is the solar irradiance of the ground, and A the solar absorption.

2. Liou, K.N. (1976) On the absorption, reflection and transmission of solar radiation in cloudy atmospheres, J. Atmos. Sci. 33:798-805.
3. Bunting, J.T. (1979) Personal communication.

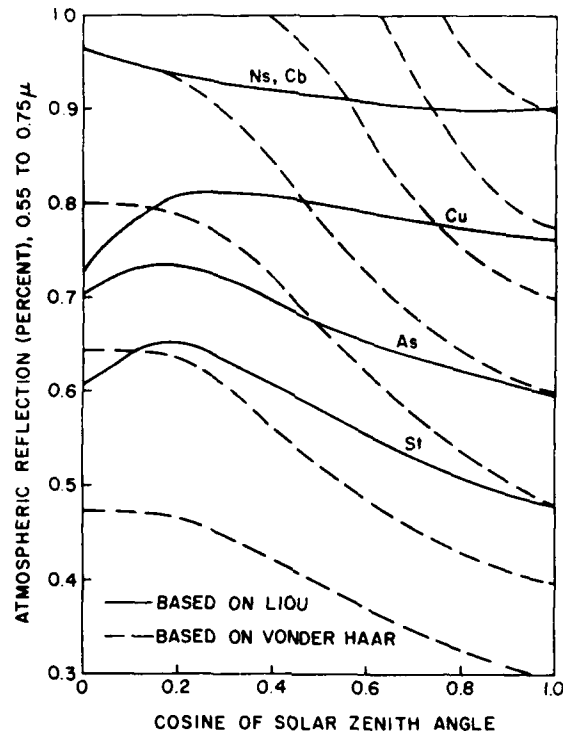


Figure 2. Atmospheric Reflection at 0.55 to 0.75 μ as a Function of Solar Zenith Angle for Four Cloud Models, and Lines Depicting $f(\xi)$

Now, \tilde{N}^* is known, and \tilde{H}_g can be measured, but we still need \tilde{A} . The data of Liou^{2*} indicate that $\tilde{A}/\tilde{H}^* \simeq 1/3 \bar{A}/\bar{H}^*$. With use of this relation and data in the same figures, the following empirical relation was developed:

$$\tilde{r}_c \simeq 1.98 - (1 - 3\bar{H}_g/\bar{H}^* \cos \xi) \quad (10)$$

With the satellite measuring \tilde{N} and the ground-based radiometer measuring \tilde{H}_g , we need only \tilde{N}_g to compute χ . Intuitively we would expect this to be small, but while we cannot measure the value, we can, however, make a rough estimate. The light passing through the clouds from the ground is the incident light reaching the ground times the albedo times an attenuation factor that is a function of a path length to the satellite. Thus

* Particular reference is made to Liou's Figures 4, 5, and 6.

$$\frac{\bar{N}_g}{\bar{N}_0 \cos \zeta} = a \left(\frac{\bar{H}_g}{\bar{H}^* \cos \zeta} \right) a^{1/\cos \theta} \quad (11)$$

where a is the attenuation factor, which is related to the light reaching the ground by,

$$a = \left(\frac{\bar{H}_g}{\bar{H}^* \cos \zeta} \right)^{\cos \zeta} \quad (12)$$

For a forested area,⁴ a typical albedo would be 0.15; at a latitude of 42 degrees in northeast United States, θ , the satellite zenith angle, is about 48 degrees, and we have

$$\frac{\bar{N}_g}{\bar{N}_0 \cos \zeta} = 0.15 \left(\frac{\bar{H}_g}{\bar{H}^* \cos \zeta} \right)^{1+1.5 \cos \zeta} \quad (13)$$

Here $\bar{H}_g/\bar{H}^* \cos \zeta$ is typically 0.4 or less with overcast conditions (except for thin cirrus). Therefore $\bar{N}_g/\bar{N}_0 \cos \zeta$ would be 0.01 or less, and the value for the satellite spectral range would likewise be very small.

To compute values of χ , simultaneous satellite video data and ground-based radiometer data were collected for the period April 1977 through October 1977, at Otis AFB, Massachusetts. Computations of χ were made for cases with $\tilde{r} \geq 0.5$ (opaque clouds); χ was then plotted against solar zenith angle for each hour, and smooth curves drawn. Values of χ were extracted from the curves and plotted on a diagram of solar elevation and azimuth angles, as shown in Figure 3. In preparing the diagrams, we assumed symmetry about local noon. To extend the data sample, we obtained hourly radiation values for Burlington, Vermont, from the National Oceanic and Atmospheric Administration (NOAA), repeating the procedure to obtain the values of χ shown in Figure 4. Both the magnitudes and patterns are quite similar. The large values near elevation 45 degrees and azimuth 70 degrees indicate minimum satellite radiance; these values are in a geometrical position where Mie scattering from cloud droplets should produce relatively low values (beyond the "cloud-bow"). To the left we might expect low values of χ where the cloud-bow should be, but the position of the bow varies with both drop-size and wavelength; this could easily be smoothed out (the relative maximum of χ would be much broader). At zero azimuth angle and elevation angle of about 41 degrees, we

4. Hummel, J.R., and Reck, R.A. (1979) A global surface albedo model, J. Appl. Meteorol. 18:244.

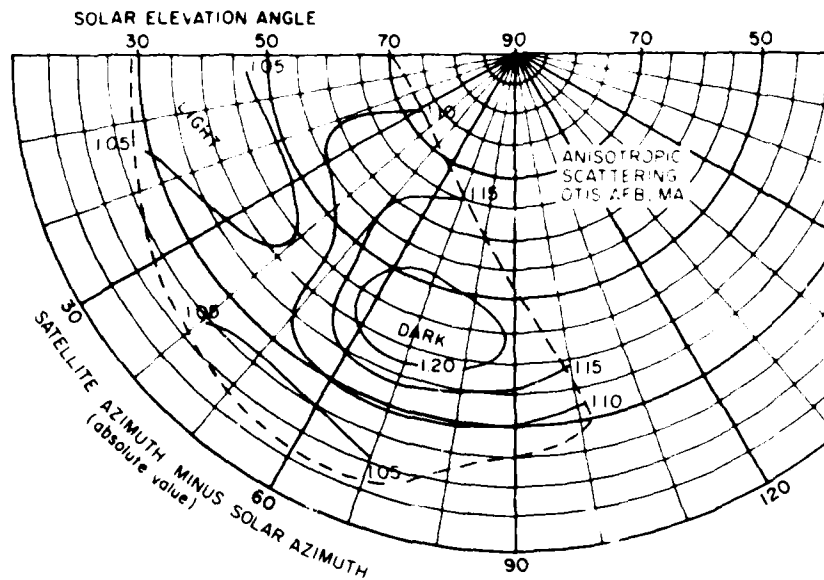


Figure 3. Anisotropic Scattering Function for Bright Clouds, Based on Surface Radiation Data at Otis AFB, Massachusetts, and GOES Video Data

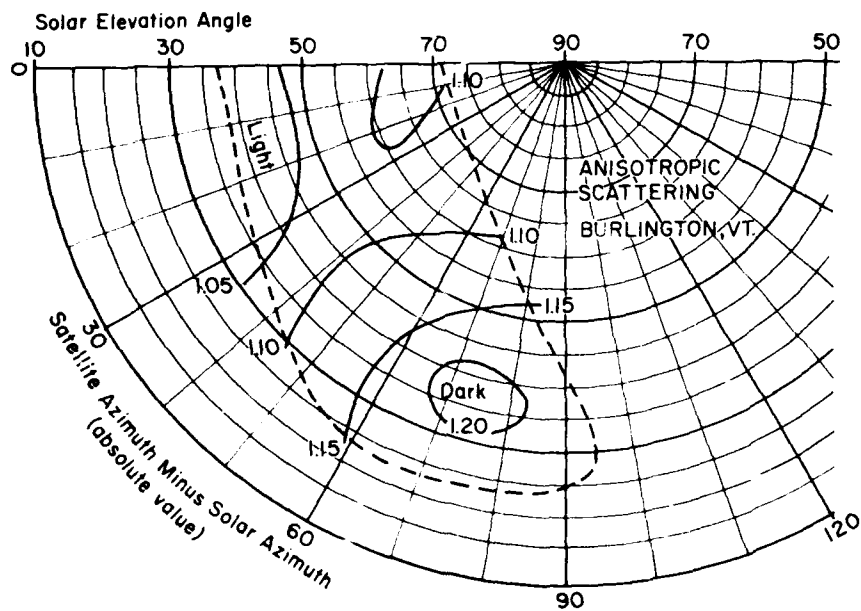


Figure 4. Anisotropic Scattering Function for Bright Clouds, Based on Surface Radiation Data at Burlington, Vermont, and GOES Video Data

should see low values of χ corresponding to the "glory." A "light" area (low χ values) is found here on both diagrams, but the area is much larger than the glory should be (no more than a degree or two). Perhaps the glory is smeared by ice crystal clouds above the water droplet clouds. While the resolution in the Sikula and Vonder Haar data is coarse, their data do not seem to show such patterns.

It is a little disturbing that the high values of χ near the 70 degrees azimuth do not arc around the glory point as would be expected from physics of scattering. This may mean that the algorithm relating zenith angle to total scattering is incorrect at high and low zenith angles which, in turn, would mean that the χ values in Figures 3 and 4 are also incorrect. However, the algorithm and the values of χ are linked by real satellite data and the two combined (algorithm and χ) are at least consistent and should be reliable when used together.

An algorithm to compute normalized reflectivity is given in Appendix B.

3. BRIGHTNESS ANALYSIS

In the interim report⁵ on this investigation, an analysis was made of the brightness of the earth's surface as measured by the satellite during clear sky conditions. In actuality, it was not brightness in the strict physical sense that was analyzed, but the digital count of the visual sensor which is proportional to the square root of the albedo. The ground-surface analysis was made in order to evaluate the temporal and spatial stability of the data, and to identify the brightness characteristics of surfaces under cloud-free conditions, operationally important information in itself.

3.1 Ground Brightness

Four stations were selected for a pilot study of the background brightness: Bedford, Massachusetts, Albany, New York, Pittsburgh, Pennsylvania, and Dulles International Airport, Virginia. The statistical sample was based on the digital counts from a 27×27 (729) pixel box centered at each of the four stations. This sample covered approximately a 26×35 mile area on the earth. Each 27×27 -pixel box was subdivided into nine boxes of 9×9 (81) pixels each. These 81-pixel boxes were each further subdivided into 7×7 , 5×5 and 3×3 pixel boxes. Figure 5 illustrates this geometry. For each of these subdivisions and the entire 729-pixel box, the mean, standard deviation, maximum, minimum and range of digital count were computed and tabulated. Statistical data for observations of

5. Keegan, T.J. (1978) Variation in Ground Brightness Over Northeastern United States as Sensed by GOES Satellites, AFGL-TR-78-0290, AD A068 085.

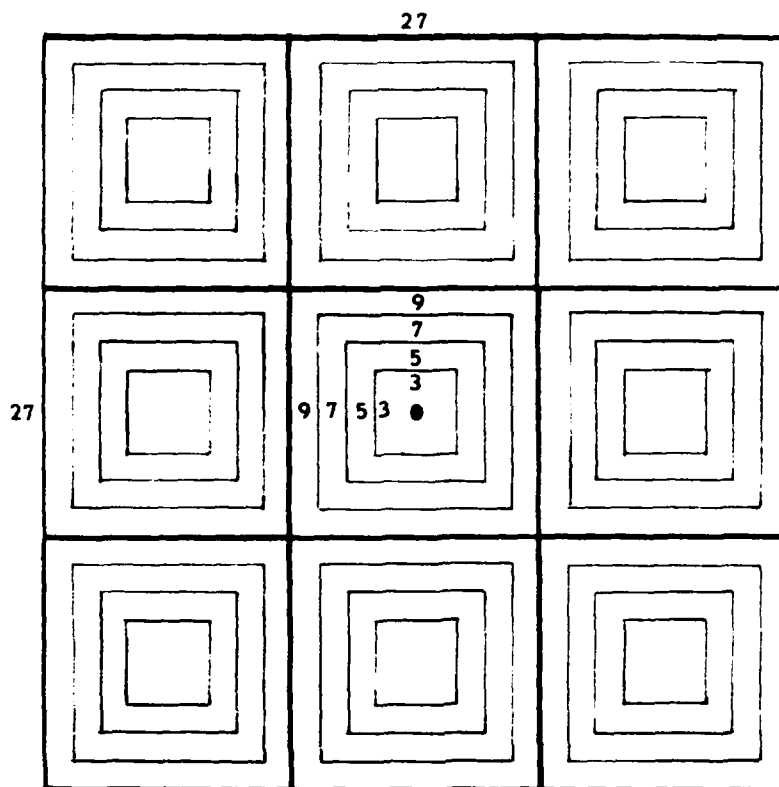


Figure 5. Geometric Arrangement of Grids Used in Computing Statistics from Video Imagery Data in Vicinity of Test Stations

clear skies were extracted and analyzed. We not only excluded data when visibility restrictions were reported (for example, haze) but also afternoon data when thick or persistent haze had been reported in the morning. Examination of both digital and hard-copy data revealed that in these cases the base of the haze layer just moved aloft although it was still apparent in the satellite data as brighter values.

3.2 Local Variations in Ground Reflectance

Albedo α can be related to digital count C through the relationship⁶

$$\alpha = 0.2 \left(\frac{C}{k} \right)^2 \quad (14)$$

6. Bristor, C.L., Ed. (1975) Central Processing and Analysis of Geostationary Satellite Data, NOAA-TM-NES-64, Washington, D.C.

where k is the calibration constant relating signal to count. Dividing Eq. (14) by the cosine of the zenith angle to normalize α for solar elevation and replacing $k^2/0.2$ by a single constant, we reduce Eq. (14) to Eq. (3) for Lambertian reflectance.

Table 2 lists reflectance statistics for four clear days in the spring of 1977 at 1600Z for various size areas centered on Bedford. Visibility on 29 April and 3 May was reported as 20 miles and on the other two days as 15 miles. The column labeled 1 gives the reflectance of the pixel at Bedford. The statistics are very stable in respect to sample size and date. Only the range value on 12 May looks out of place for the 729-pixel box, since it is more than twice as much as on the other days. Examination of the individual pixels revealed the presence of several bright spots in the upper-right hand corner of the satellite array, which were caused by the first elements of a cloud, moving into the area and not yet detectable by the Bedford observer. The number of pixels involved was so small that even the standard deviation was not noticeably affected. In contrast to the ground values shown in Table 2, bright clouds would have reflectances of 0.6 and some clouds associated with precipitation, 0.8 or more.

Table 2. Reflectance Statistics for Clear Days in Vicinity of Bedford, Massachusetts, at 1600 UT, as a Function of Area, on 29 April; 3, 12, and 23 May 1977

Type	Number of Pixels					
	1	9	25	49	81	729
Average						
29 April	0.11	0.10	0.10	0.10	0.10	0.10
3 May	0.12	0.11	0.10	0.11	0.11	0.11
12 May	0.12	0.11	0.11	0.11	0.10	0.10
23 May	0.10	0.10	0.10	0.10	0.10	0.10
Standard Deviation						
29 April		0.005	0.008	0.008	0.008	0.009
3 May		0.010	0.010	0.009	0.009	0.008
12 May		0.012	0.011	0.009	0.009	0.010
23 May		0.004	0.006	0.007	0.007	0.007
Range						
29 April		0.02	0.04	0.05	0.05	0.06
3 May		0.03	0.03	0.03	0.04	0.05
12 May		0.04	0.04	0.04	0.04	0.17
23 May		0.01	0.02	0.03	0.04	0.05

Table 1 presents the same basic data in a different format. Here the statistics are computed for each of the nine 81-pixel boxes that make up the 10-ft \times 10-ft array. The boxes in the table correspond to the nine heavily ruled boxes in Figure 1. Again the values are consistent in all directions from Bedford. The onset of the initial over-saturation of 1 axis into the area on 12 May can be seen in the standard deviation and maximum values in the upper right-hand box.

The evidence presented in Tables 2 and 3 is very encouraging. It shows that, at least at the low end of the brightness scale, the data are stable. From place to place, and over a wide range of sample sizes, the reflectance statistics are consistent with the homogeneity of the surface.

Table 2. Reflectance Statistics Over 9 \times 9 Pixel Areas Surrounding Bedford, Massachusetts, at 1600 UT, for Selected Clear Days in 1977

Area 1					Area 2				Area 3					
Area	Mean	Max	12 May	20 May	Area	Mean	Max	12 May	20 May	Area	Mean	Max	12 May	20 May
75 \times 75	0.10	0.10	0.10	0.10	75 \times 75	0.10	0.11	0.10	0.10	75 \times 75	0.10	0.11	0.11	0.10
125 \times 125	0.09	0.09	0.09	0.09	125 \times 125	0.011	0.009	0.008	0.008	125 \times 125	0.010	0.009	0.011	0.008
225 \times 225	0.11	0.11	0.11	0.11	225 \times 225	0.11	0.13	0.12	0.12	225 \times 225	0.11	0.12	0.12	0.11
325 \times 325	0.07	0.07	0.07	0.07	325 \times 325	0.07	0.09	0.08	0.08	325 \times 325	0.07	0.08	0.08	0.07
425 \times 425	0.04	0.04	0.04	0.04	425 \times 425	0.04	0.04	0.04	0.04	425 \times 425	0.04	0.04	0.04	0.04
525 \times 525	0.10	0.10	0.10	0.10	525 \times 525	0.10	0.11	0.10	0.10	525 \times 525	0.10	0.11	0.10	0.10
625 \times 625	0.008	0.008	0.008	0.008	625 \times 625	0.008	0.009	0.009	0.007	625 \times 625	0.012	0.008	0.009	0.008
725 \times 725	0.12	0.12	0.12	0.12	725 \times 725	0.12	0.12	0.12	0.12	725 \times 725	0.13	0.13	0.13	0.12
825 \times 825	0.09	0.09	0.09	0.09	825 \times 825	0.07	0.09	0.08	0.08	825 \times 825	0.07	0.09	0.09	0.09
925 \times 925	0.04	0.04	0.04	0.04	925 \times 925	0.04	0.03	0.04	0.04	925 \times 925	0.06	0.04	0.04	0.04
1025 \times 1025	0.10	0.11	0.10	0.10	1025 \times 1025	0.10	0.10	0.10	0.10	1025 \times 1025	0.11	0.11	0.10	0.10
1125 \times 1125	0.008	0.007	0.009	0.008	1125 \times 1125	0.008	0.007	0.009	0.007	1125 \times 1125	0.008	0.007	0.009	0.008
1225 \times 1225	0.12	0.12	0.12	0.12	1225 \times 1225	0.12	0.12	0.12	0.12	1225 \times 1225	0.12	0.12	0.12	0.12
1325 \times 1325	0.09	0.09	0.09	0.09	1325 \times 1325	0.08	0.09	0.09	0.08	1325 \times 1325	0.08	0.09	0.09	0.08
1425 \times 1425	0.04	0.03	0.03	0.04	1425 \times 1425	0.04	0.03	0.03	0.04	1425 \times 1425	0.04	0.03	0.03	0.04

3.3 Time Variations in Ground Reflectivity

One of the initial tests of the data was to examine, on cloudless days, the relationship of the digital count to the solar elevation angle. The average count in a 729-pixel box was analyzed on a monthly basis. Correlation coefficients of the count as a function of solar elevation were above 0.90. Figure 6 summarizes the month to month count variation deduced from the data gathered for the four stations. The geographical separation among the four stations yields some large time differences between the spring appearance and the fall turning of foliage. Despite the station grouping and the fact that at least half the months had an insignificant number of points, the regression lines display a great amount of orderliness. The slopes flatten and the background darkens from spring to summer and then reverses

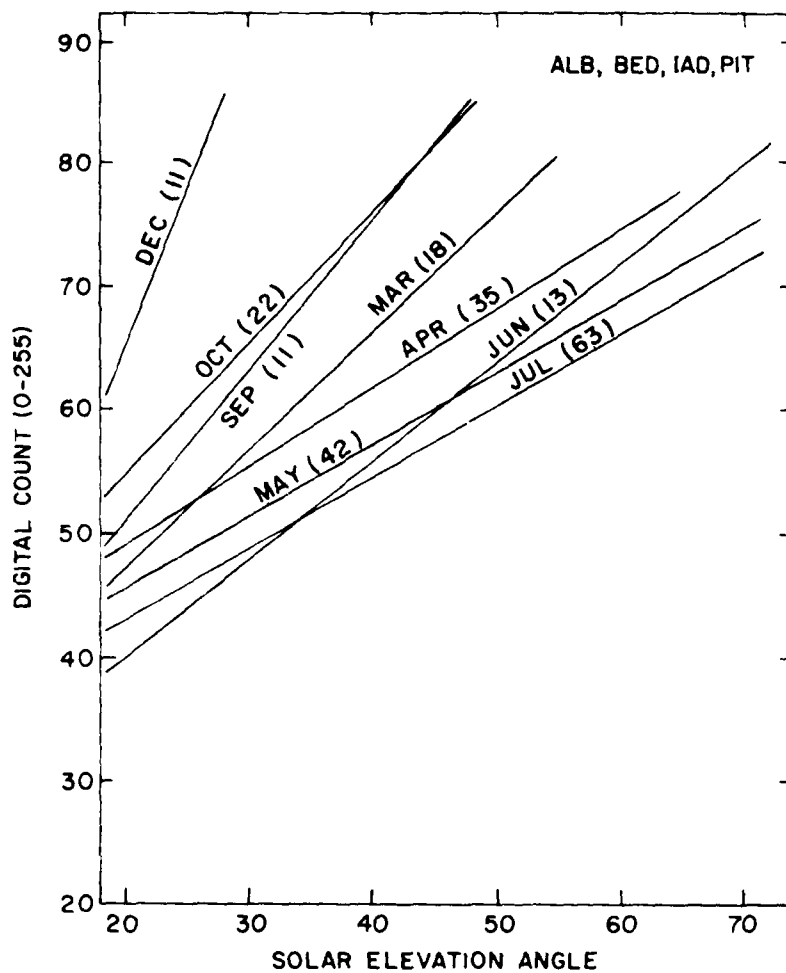


Figure 6. Monthly Variation of Average Brightness (Video Count, 0-255) as a Function of Solar Elevation Angle

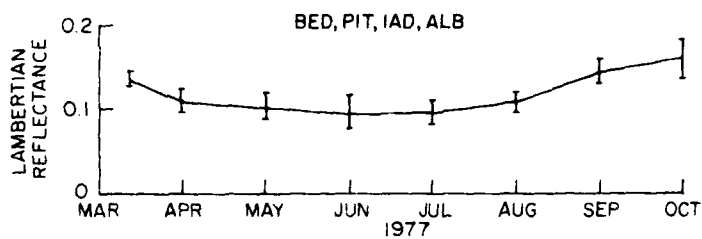


Figure 7. Clear-sky Reflectance of the Ground at Four Locations (Bedford, Massachusetts, Pittsburgh, Pennsylvania, Dulles International Airport, Virginia, and Albany, New York) as a Function of Month

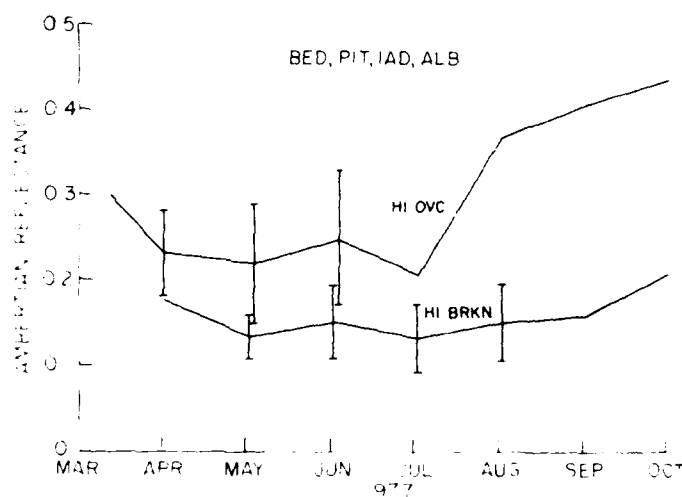
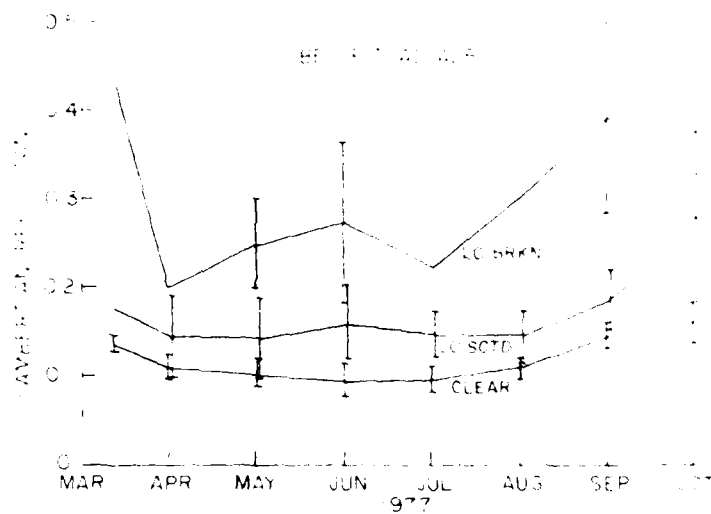


Figure 8. Reflectance Sensed by GOES under Conditions of:
 (a) Clear skies, low scattered clouds, and low broken clouds;
 (b) high broken clouds and high overcast clouds, as a function of month

of the data is small. The details of these calculations will be given in a later report. However, some comments may be made at this point. Such quantities as reflectance, as well as standard deviation, are a function of the stability of the sensor. Correcting the digital count values used to construct Figure 6 to Lambertian reflectance values through Eq. (14) and plotting the result produces Figure 7. The reflectances generate a fairly smooth curve showing a seasonal variation and with standard deviations that are small. The magnitude of the seasonal variation, however, is subject to some reservation at this point. The effects of anisotropic scattering, as noted in Section 2.3 of this report, may require that the digital counts be corrected for bidirectional reflectance to represent hourly, seasonally and geographically consistent quantities.

3.4 Time Variations in Cloud Reflectivity

A pilot test was made of the seasonal variation in the Lambertian reflectance of low scattered, broken and high broken, and overcast clouds. These conditions were selected because we could be reasonably certain that they consisted of the single layer reported in the hourly observations. A single layer of high scattered clouds is usually indistinguishable, in the digital count, from clear conditions³ and these cases were not included. Figures 8a and 8b show the results. The "clear" curve from Figure 7 is repeated in Figure 8a for reference. The two classes of low clouds and the two classes of high clouds have reflectances that are distinct from each other and from clear. Even the standard deviations have very little overlap. On the contrary, the low scattered and high broken and the low broken and high overcast curves closely duplicate each other. At this point in the study, these ambiguities do not constitute a serious concern. Statistics other than the mean and the addition of infrared temperature data as a cloud specifier should easily separate these simple cases.

4. ESTIMATION OF RAINFALL RATE USING GEOSYNCHRONOUS SATELLITE IMAGERY DATA

The most obvious application of satellite imagery information is to the specification of cloudiness, since clouds produce the relatively bright returns in the visible wavelengths channel and the cool returns in the IR channels. However, meteorologists have noted that the brightest and the coolest of the clouds were most apt to be associated with precipitation at the ground. A relationship between satellite imagery and surface precipitation would be very useful in weather analysis and forecasting, as the imagery has far greater spatial resolution than conventional data and more complete and uniform coverage than radar data. More complete

precipitation depiction would not only improve precipitation forecasting but it would also lead to better forecasts of ceiling and visibility, which usually lower during periods of precipitation.

Intuitively, one should expect bright clouds to be associated with precipitation, for, under these conditions most light is scattered above clouds and little light remains to reach the ground. For centuries, man has known that darkening skies foretell rain, and the darker, the heavier the rain. However, until recent years it has been relatively difficult to assess quantitatively the relationship of satellite observations to rainfall rate because early data were in uncalibrated analog form and because positioning errors were large, often as large as the horizontal dimensions of a good shower. The geosynchronous satellites improved this situation, since they provide calibrated digital output, half-hourly images, and improved navigation capability. This section will describe an effort to estimate rainfall rates from satellite measurements, starting with a confirmation experiment that precipitation rate is related to sky brightness as measured at the ground (darkness when seen from the ground), and then to relationships of cloud brightness and infrared temperature to rainfall rate.

4.1 Rainfall Rate and Sky Brightness

While the satellite data were being archived, a short investigation was made to verify quantitatively the relationship between sky brightness (or darkness) and rainfall rate, inferring the brightness the satellite would measure. A special weather test facility has been set up by AFGL, located at Otis AFB on Cape Cod, Massachusetts.⁷ Among the many sensors routinely recorded on magnetic tape are two total sky radiometers, a direct-sun pyrheliometer and a tipping-bucket rain gauge with 0.005 in. (0.13 mm) sensitivity. The three radiation sensors respond to light in the range 0.2 to 3.5 microns.

To estimate the light being scattered up to a satellite, we start by solving the solar flux equation for upward scattered radiation. Thus:

$$F_c^* = \bar{H} * \cos \xi - \bar{H}_g - \bar{A} \quad (15)$$

(the contribution from surface albedo is considered negligible under overcast conditions). While the absorption \bar{A} is not easy to determine, as noted in Section 2.3, Liou² has published data on atmospheric reflection, absorption and transmission using several model clouds (stratus, altostratus, nimbostratus, cumulus, and

7. Chisholm, D.A. (1978) Weather Automation Studies at the Otis Weather Test Facility, Preprint Volume: AMS Conference on Atmospheric Environment of Aerospace Systems and Applied Meteorology, Nov 14-16, 1978, 196-200.

cumulonimbus). For all but the cumulus, we can closely approximate the atmospheric reflectivity by:

$$\bar{r} = \bar{F}^*/\bar{H}^* \cos \xi \approx 1 - (0.01 + 0.9 \bar{\Pi}_g \bar{H}^* \cos \xi)^{1/2} \quad (16)$$

However, we should note that this approximation is not valid for solar zenith angles greater than 80 degrees ($\cos \xi < 0.2$). This expression includes the effect of sun angle on the incident solar radiation, but \bar{r} varies further with zenith angle due to scattering paths, and thus we can normalize to overhead zenith angle using the approximation

$$\bar{r}_0 \approx 1.09 - 2(1.09 - \bar{r})/(1 + \cos^{1/2} \xi) \quad (17)$$

which was also derived from the data of Liou² (see Eq. (7), Section 2.3).

During the period March through September 1977, 5-min mean values of \bar{H}_g were extracted on the hour and half hour, along with the corresponding 5-min precipitation rate from the tipping-bucket rain (0.005 inch or 0.13 mm per tip). Some 293 observations with dense cloud ($\bar{r} > 0.40$) were collected. Reflectivity \bar{r} was computed for each observation and normalized to overhead sun, using the Eq. (17). Then, the probability of exceeding each of five thresholds of rainfall rate was computed as a function of normalized reflectivity. The resulting curves are shown in Figure 9. The plotted points are based on 35 to 50 observations, with exception of 20 available at $\bar{r}_0 = 0.82$, and only 4 at 0.85. Therefore, the curves beyond 0.82 are dashed lines as the sample is too small to yield reliable probability estimates.

The curves do confirm that rainfall rate and cloud reflectivity are related. Moreover, the relationship is quite sensitive to the reflectivity; for example, at a constant probability of 40 percent, there is a factor of 3 increase in rainfall rate for each 0.05 increase in reflectivity. To detect such small differences from a satellite, requires not only stable satellite sensors but also careful corrections for anisotropic scattering.

4.2 Surface Visibility and Sky Brightness

On a number of occasions, we noted that the Otis WTF total downward radiation measurements was lower on hazy days (visibility 6 miles or less) than on good clear days (visibility 20 miles or more). An example is shown in Figure 10. This would imply that more sunlight is scattered out to space on hazy days and the haze might be detectable (and visibility estimated) from satellite data. The upward scattered radiation \bar{F}_c^* is given by

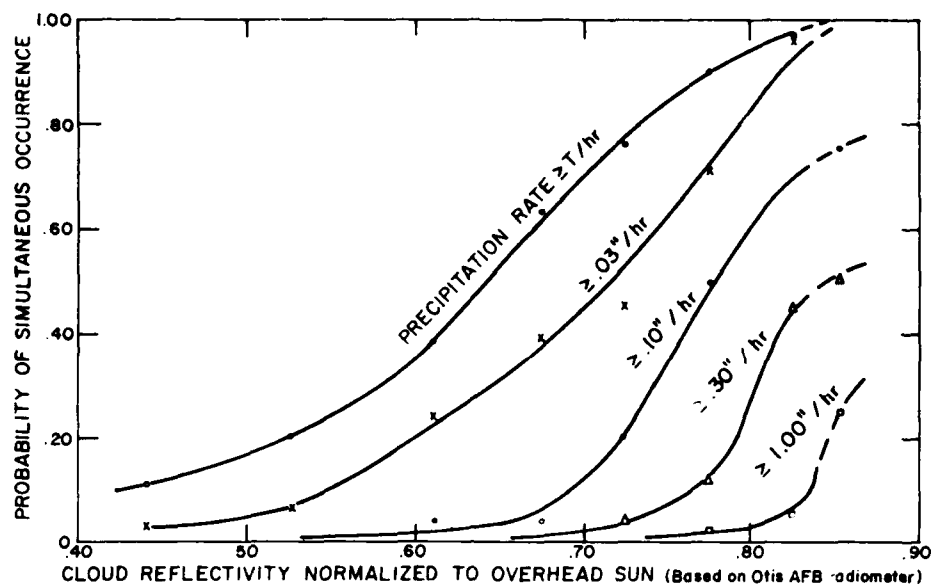


Figure 9. Probability of 5-min Precipitation Rate Versus Cloud Reflectivity, for $\geq \text{trace}$, for ≥ 0.03 in. (0.8 mm), for ≥ 0.10 in. (2.5 mm), for ≥ 0.30 in. (1.6 mm) and for ≥ 1.00 in. (25.4 mm) per hour

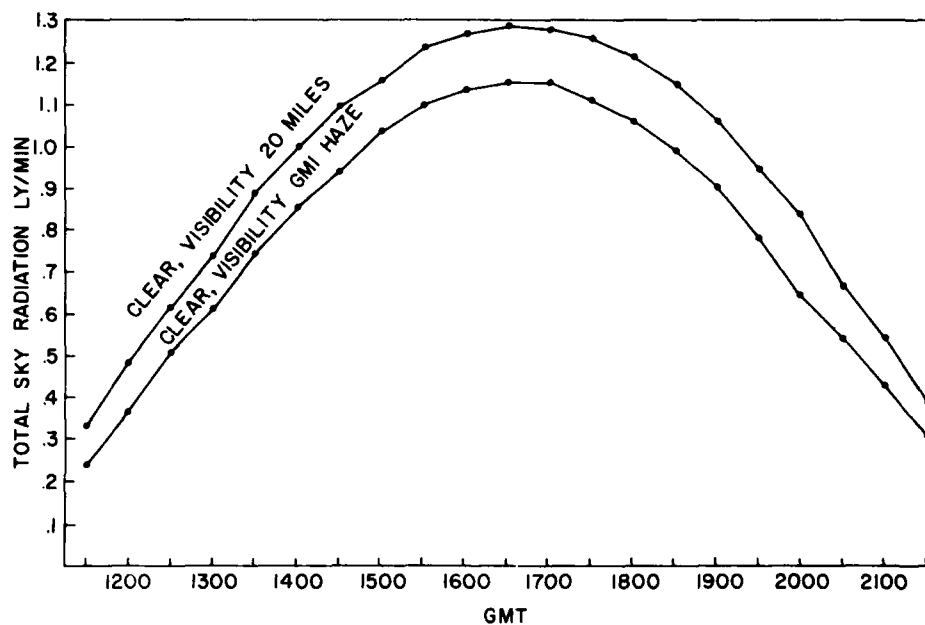


Figure 10. Effect of Haze on Total Radiation at the Surface, in mid-April 1977, at Otis AFB, Massachusetts

$$\bar{F}_c^* = \bar{H}^* \cos \zeta - \bar{H}_g - \bar{A} \quad (18)$$

If we look at the difference that is seen in Figure 10, we have

$$(\bar{F}^*)_{\text{hazy}} - (\bar{F}_c^*)_{\text{clear}} = (\bar{H}_g)_{\text{hazy}} - (\bar{H}_g)_{\text{clear}} - (\bar{A})_{\text{hazy}} + (\bar{A})_{\text{clear}} \quad (19)$$

Around noon in our example, the difference in \bar{H}_g is about $0.13 \text{ cal/cm}^2 \text{ min.}$ Obtaining total moisture from radiosonde data, we can use Table 147 (Transmission of Solar Radiation Through Moist Air) in Smithsonian Meteorological Tables⁸ to compute differences in absorption as $0.04 \text{ cal/cm}^2 \text{ min.}$ Thus the increase in \bar{F}^* would be $0.09 \text{ cal/cm}^2 \text{ min.}$ The total upward scattering, \bar{F} would be

$$\bar{F} = \bar{F}^* + \bar{\alpha} \bar{H}_g \quad (20)$$

For this example, if we have a forested background with 0.15 albedo,⁴ and a typical upward-scattered clear sky reflectivity of 10 percent, the net upward scattering would be about $0.32 \text{ cal/cm}^2 \text{ min.}$ Thus, the haze would result in an over-all increase in upward scattering of about 28 percent for the whole visible spectrum. The small-particle dry-hazes scatter relatively more in the blue portion of the spectrum than do the "whiter" water droplet clouds, but hazes scatter less in the red portion. In the middle, in area of the satellite measurement, the difference would be small and a 28 percent increase would be a valid estimate. However, we must consider that the GOES video transmission consists of "counts," namely, integers from 0 to 63, that are proportional to the square root of radiance. A typical clear ground value would be about 18 and the haze would increase this value to only about 20 or 21, which might be missed if one were not looking for small differences. As in the case of rainfall rate, one must have a stable satellite sensor and good corrections for changing sun angle, in order to detect haze consistently against a clear ground.

4.3 Specification of Rainfall from Satellite Imagery Data

In Section 4.1, there is evidence that rainfall rate is related to the darkness of the sky as seen from the ground and, with some reasonable assumptions, the rainfall rate is shown to be related to the brightness of the clouds as seen from above. Studies have been made to develop relations between satellite imagery

8. List, R.J. (1951) Smithsonian Meteorological Tables, Sixth Revised Edition, 1951.

data and rainfall,^{9, 10} but primarily for tropical latitudes and convective storms. However, similar relations should exist for higher latitudes and for nonconvective clouds.

Originally, a search for such relations was planned using data from the sensitive rain-gauge (0.005 inch or 0.13 mm per tip) located at the AFGL facility, Otis AFB, used in the study in Section 4.1. When the satellite and rainfall data for the period April through November of 1977 were assembled, gaps appeared in both sets of data, which did not overlap; the combined sample was rather small, particularly for the higher rainfall rates.

As an alternative, hourly rainfall records were obtained from Local Climatological Data¹¹ summaries for stations in the northeast United States. From this group, five stations, representing varying topography, were selected: Burlington, Vermont, Buffalo, New York, Pittsburgh, Pennsylvania, Charleston, West Virginia, and Atlantic City, New Jersey. We should note that individual satellite data counts represent essentially "instantaneous" values, obtained from scanning a point for only a few microseconds. Fortunately, heavy clouds usually are persistent for periods up to an hour or more, so that the satellite values should be temporally compatible with the one-hour rainfall measurements. (Obviously, we would have preferred five-minute samples using the rain gauge at Otis AFB.)

Radar meteorologists and cloud physicists have long known that cloud systems with high tops (hence "cold" due to adiabatic expansion) are associated with greater precipitation rates. Satellite meteorologists (for example, Lethbridge¹²) soon found that low temperatures seen by the IR "window" channel of the satellite were often associated with significant precipitation. While the primary goal in this section was to find relationships between the video brightness and rainfall rate, there was good reason to believe that the IR brightness or "temperature" would also be related to rainfall rate. Thus, imagery data from the GOES IR channel was included in this study, in order to see to what extent it might complement the video data for the production of a better specification.

-
9. Griffith, C.G., Woodley, W.L., Browner, S., Teirjeiro, J., Maier, M., Martin, D.W., Stout, J., and Sikdar, D.N. (1976) Rainfall Estimation from Geosynchronous Satellite Imagery During Daylight Hours, NOAA Technical Report ERL-356-WMP07, 106.
 10. Scofield, R.A. (1978) Using Satellite Imagery to Estimate Rainfall During the Johnstown Rainstorm, AMS Preprint, Conference on Flash Floods: Hydrometeorological Aspects (181-189).
 11. Local Climatological Data, Monthly Summary, April-November 1977, NOAA Environmental Data Service.
 12. Lethbridge, M. (1967) Precipitation Probabilities and Satellite Radiation Data, Monthly Weather Review 95:487-490.

4.4 Data Extraction and Processing

As noted in Section 2.2, the satellite data available from our archive consist of hourly images in the area from Michigan to Nova Scotia and from Maine to North Carolina. To allow for experimentation with spatial averaging, video values were averaged over 7-km (4 mi) squares and a 65-point array (8×8 plus center point) of data were extracted from over each of the five chosen stations. Since the IR data from GOES have coarser resolution, 17-point arrays (4×4 plus center point) for 14-km squares were extracted. These arrays were taken from images during the period April through November 1977. The sample of 552 cases for each of the five stations includes fair weather and nonprecipitating clouds as well, so that the sample would not be biased towards hours when rain was actually reported on the ground.

In the processing of the data, the four nearest 7×7 km video data points were averaged to be compatible with the 14×14 km IR value over the station. The video values were normalized for sun angle, following previously described procedures in order to obtain a normalized reflectance or "brightness." The IR value was modified only by converting to temperature, according to Corbell, Callahan and Kotsch.¹³ For each pair of video brightness and IR temperature, the rainfall for the following hour was extracted from the National Climatic Center data sheets (Local Climatological Data¹¹). A first thought was to average the satellite values at the beginning and end of the hour. However, cloud and precipitation particles seen by the satellite are near the top of the cloud, requiring some time before reaching the ground. For example, small raindrops would take about 15 min to fall from a 4-km height. Thus, it would be physically more realistic to use only the satellite data at the beginning of the hour, when comparing to hourly rainfall amounts. An added advantage of this procedure is that we are not only specifying surface precipitation, but actually making a short-range forecast.

In the next step, the one-hour rainfall amounts were plotted on a diagram with IR cloud temperature as the abscissa and normalized video brightness (cloud reflectivity) as the ordinate. A grid with intervals of 10 C and 0.10 brightness was overlaid and the following statistics computed for each box: number of events ≥ 0.01 in. (0.25 mm), ≥ 0.10 in. (2.54 mm), the mean rainfall and standard deviation. The grid was offset by 5 C and 0.05 brightness and the procedure repeated. Computed frequency of occurrence and mean rainfall were then plotted at the centers of the grids on similar diagrams of temperature versus brightness and smooth isopleths drawn through the fields. The resulting charts portraying rainfall amount,

13. Corbell, P., Callahan, C., and Kotsch, W.J. (1978) The GOES/SMS Users Guide, NOAA National Environmental Satellite Service, (Ref App II Attachment A3).

probability of ≥ 0.01 inch, and probability of ≥ 0.10 inch are shown in Figures 11, 12, and 13, respectively. While these diagrams stop at -10°C and 0.5 reflectivity, there were many points beyond, though so few with precipitation that the average amount was essentially zero and the probabilities close to zero.

4.5 Results

Figures 11, 12, and 13 were each based on 300 observations of rainfall amount, with values ranging from zero to 0.66 in. (16.8 mm). In all, this amounts to 8.50 in. (216 mm) or about 7 percent of what fell on the five stations in the seven-month period of the sample. With six to eight images being archived each week-day, we had hoped for as high as a 20 percent "capture," but unfortunately there were McIDAS hardware difficulties during a six-week period in August and September, the two rainiest months of the sample.

The relationships shown on these diagrams (Figures 11, 12, and 13) are essentially as expected: high rainfall rate associated with low IR temperature and high brightness (reflectivity). The most useful probability diagrams for specification or prediction have large areas of both very high and very low probability, separated by a small area with tightly-packed probability isopleths. In Figure 12, there are some moderately high and moderately low probability regions, but nothing approaching 95 percent and 5 percent; in Figure 13 the probabilities range from low (about 40 percent) to very low (about 1 percent). The separation on both diagrams is far from ideal, but the diagrams would still be useful for making decisions if the threshold for "action" versus "no action" is known.

The computed standard deviations indicate that there is considerable uncertainty in the specification of rainfall amount as shown in Figure 11. This uncertainty can best be expressed as a factor of about 2.5; that is, for a one-hour rainfall specification of 0.10, two-thirds of the values would fall between 0.25 and 0.04. By way of comparison, if one specifies hourly rainfall by temporal persistence, the error will be a factor 2.5 in about two hours, or, if one uses spatial extrapolation, about 50 to 100 km (these times and distances will be larger in winter and smaller in summer). Weather radar¹⁴ can specify rainfall over a point within a factor of 2, 75 percent of the time, somewhat better than the satellite-based specification using dependent data.

One should note that both video and IR information are important in defining this relationship shown in Figures 11 through 13 and there would, obviously, be considerable loss in accuracy if either one were omitted. In particular, at night, when only IR is available, observations of cold temperatures could be misleading,

14. Wilson, J., and Brandes, E. (1979) Radar Measurement of Rainfall - A Summary, AMA Bulletin, 60:1048-1058.

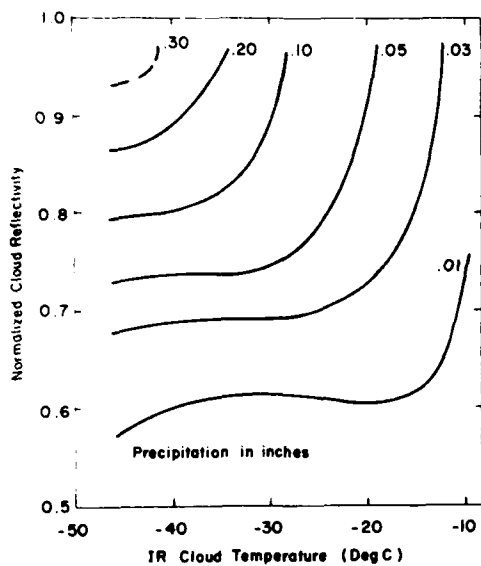


Figure 11. One-hour Rainfall as a Function of Normalized Cloud Reflectivity and Infrared Cloud Temperature

Figure 12. Probability of One-hour Rainfall ≥ 0.01 in. (0.25 mm) as a Function of Normalized Cloud Reflectivity and Infrared Cloud Temperature

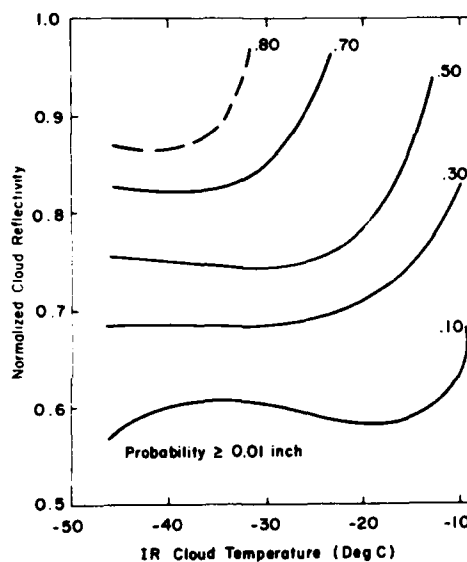
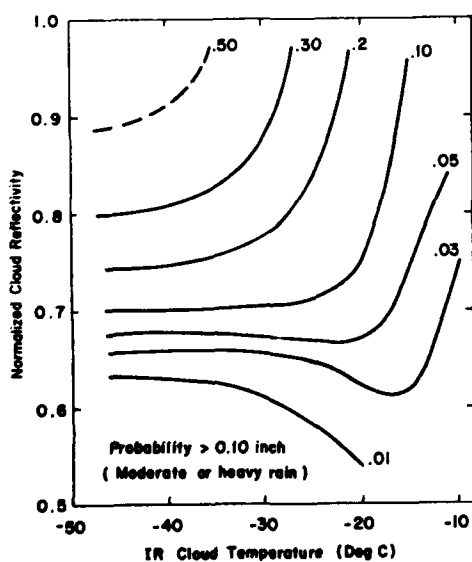


Figure 13. Probability of One-hour Rainfall ≥ 0.10 in. (2.54 mm) as a Function of Normalized Cloud Reflectivity and Infrared Cloud Temperature

if they were due only to cirrus clouds without the clouds beneath that would lead to high video brightness.

At brightnesses greater than 0.85 and IR temperature less than -35 C, there were only 10 points and thus the isopleths in this area are shown as dashed lines since the values were considered tentative.

4.6 Potential Specification Improvements

There are, of course, many ways in which the specification can be improved, and some of these will be explored in future studies. Different spatial averaging or use of satellite observations other than the one over the rain gauge might help. Additional information such as spatial variability of brightness and IR temperature would provide an index of convection that presumably would help. Unfortunately, adding these factors reduces our degrees of freedom, and the data base must be expanded to maintain statistical reliability. In the future, we can look forward to information from other parts of the spectrum, both IR and microwave, which will be related to cloud microphysics and thermodynamics and which, in turn, is related to the precipitation process. A 6.3-micron imager (water vapor) is already present on the European METEOSAT and new sensors are planned for the future GOES.

5. CONCLUSIONS

As part of an effort to develop an automated short-range forecast capability, research has been initiated to specify surface weather conditions, given GOES digital imagery values. As a start, video and IR images over a fixed region have been routinely archived on magnetic tape since March 1977, with 2877 pairs of video and IR images recorded, to July 1979. To date, refined navigation has been performed on 1952 images. To improve the compatibility of the video data, a procedure has been developed to normalize video count values for both varying solar illumination and effects of anisotropic scattering from dense clouds. Characteristics of clear-sky background have been identified as a function of solar elevation angle and month of year. Reflectance was found to separate the low cloud conditions — clear, scattered, and broken, and also separate the high cloud conditions — clear (or scattered), broken, and overcast. Using both the satellite video and IR values, we developed a technique for specifying rainfall rate.

While the algorithms for specifying surface weather from satellite information are unlikely to be as accurate as a good (ground-based) local observation, nevertheless, the algorithms are very useful when weather information is needed for a

region devoid of surface observations. Further, when techniques are completed for the purpose of forecasting reflectivity and IR temperature through extrapolation,¹⁵ these algorithms will be necessary for conversion of the satellite values to the required weather parameters.

-
15. Muench, H.S., and Hawkins, R.S. (1979) Short-Range Forecasting Through Extrapolation of Satellite Imagery Patterns, AFGL-TR-79-0096, AD A073-081.

References

1. Sikula, G.J., and Vonder Haar, J.H. (1972) Very Short Range Local Area Weather Forecasting Using Measurements from Geosynchronous Meteorological Satellites, AFCRL-72-0260, AD 744 098, Final Report, Contract F19628-71-C-0073.
2. Liou, K.N. (1976) On the absorption, reflection and transmission of solar radiation in cloudy atmospheres, J. Atmos. Sci. 33:798-805.
3. Bunting, J.T. (1979) Personal communication.
4. Hummel, J.R., and Reck, R.A. (1979) A global surface albedo model, J. Appl. Meteorol. 18:244.
5. Keegan, T.J. (1978) Variation in Ground Brightness Over Northeastern United States as Sensed by GOES Satellites, AFGL-TR-78-0290, AD A068 085.
6. Bristol, C.L., Ed. (1975) Central Processing and Analysis of Geostationary Satellite Data, NOAA-TM-NESS-64, Washington, D.C.
7. Chisholm, D.A. (1978) Weather Automation Studies at the Otis Weather Test Facility, Preprint Volume: AMS Conference on Atmospheric Environment of Aerospace Systems and Applied Meteorology, Nov 14-16, 1978, 196-200.
8. List, R.J. (1951) Smithsonian Meteorological Tables, Sixth Revised Edition, 1951.
9. Griffith, C.G., Woodley, W.L., Browner, S., Teirjeiro, J., Maier, M., Martin, D.W., Stout, J., and Sikdar, D.N. (1976) Rainfall Estimation from Geosynchronous Satellite Imagery During Daylight Hours, NOAA Technical Report ERL-356-WMP07, 106.
10. Scofield, R.A. (1978) Using Satellite Imagery to Estimate Rainfall During the Johnstown Rainstorm, AMS Preprint, Conference on Flash Floods: Hydrometeorological Aspects (181-189).
11. Local Climatological Data, Monthly Summary, April-November 1977, NOAA Environmental Data Service.

12. Lethbridge, M. (1967) Precipitation Probabilities and Satellite Radiation Data, Monthly Weather Review 95:487-490.
13. Corbell, P., Callahan, C., and Kotsch, W.J. (1978) The GOES/SMS Users Guide, NOAA National Environmental Satellite Service, (Ref App II Attachment A3).
14. Wilson, J., and Brandes, E. (1979) Radar Measurement of Rainfall - A Summary, AMA Bulletin, 60:1048-1058.
15. Muench, H.S., and Hawkins, R.S. (1979) Short-Range Forecasting Through Extrapolation of Satellite Imagery Patterns, AFGL-TR-79-0096, AD A073 081.

List of Symbols

The symbols chosen for radiation parameters are compatible with those now used in radiation and optics. The "—" above a symbol indicates a total over the 0.2 to 3.5 micron band, and "~" indicates a total over a 0.55- to 0.75-micron band. Superscript "*" indicates a value at the top of the atmosphere.

Symbol	Description	Units
A	Atmospheric absorption of radiation	W/m^2
C	GOES video count number (0-63)	dimensionless
C _o	GOES video count number for perfect diffuse reflector and overhead sun	dimensionless
F _c	Upward radiant flux due to atmosphere (including clouds)	W/m^2
F _g	Upward radiant flux due to ground	W/m^2
G	Greenwich meridian time	hours-minutes-seconds
H _o *	Mean solar irradiance at top of atmosphere	W/m^2
H*	Solar irradiance at top of atmosphere	W/m^2
H _g	Solar irradiance at ground — direct and downward scattered	W/m^2
H _{gd}	Direct solar irradiance at ground	W/m^2
N _o	Satellite radiance looking at perfect diffuse reflector under overhead sun	$W/(m^2 sr)$

Symbol	Description	Units
N	Satellite measured radiance	$W/(m^2 sr)$
N_c	Satellite measured radiance due to atmosphere	$W/(m^2 sr)$
N_g	Satellite measured radiance due to ground	$W/(m^2 sr)$
R	Distance of earth to sun	km
R_o	Mean distance of earth to sun	km
R_s	Mean satellite orbit radius	km
R_e	Mean radius of the earth	km
a	Transmission coefficient	dimensionless
d	Julian date	dimensionless
h	Hour angle	radians
r	Cloud reflectivity	dimensionless
α	Surface albedo	dimensionless
β	Compensation factor for wavelength differences	dimensionless
γ	Arc-length observer to subsatellite point	radians
δ	Declination of the sun	radians
ξ	Zenith angle of the sun	radians
θ	Zenith angle of the satellite	radians
Ω	Solid angle	steradians
Λ	Longitude	radians
λ_s	Longitude of sub-satellite point	radians
χ	Anisotropic scattering coefficient	dimensionless
ϕ	Latitude	radians
ψ	Scattering angle between solar beam and satellite	radians
ϕ_1	Azimuth of the sun	radians
ϕ_2	Azimuth of the satellite	radians

Appendix A

Basic Equations and Satellite-Solar Geometry
(See Figures A-1 and A-2)

1. GEOMETRICAL RELATIONS

Solar azimuth angle:

$$\cos \zeta = \sin \Phi \sin \delta + \cos \Phi \cos \delta \cos h \quad (A1)$$

Solar azimuth:

$$\sin \phi = \cos \delta \sin h / \sin \zeta \quad (A2)$$

Arc-length:

$$\cos \gamma = \cos (\Lambda_s - \Lambda) \cos \Phi \quad (A3)$$

Satellite azimuth:

$$\sin (\phi_2 - \pi) = \sin (\Lambda_s - \Lambda) / \sin \gamma \quad (A4)$$

Satellite zenith:

$$\theta = \gamma + \tan^{-1} [(R_e \sin \gamma) / (R_s - R_e \cos \gamma)] \quad (A5)$$

Satellite-observer-sun angle:

$$\cos \psi = \cos \zeta \cos \theta + \sin \zeta \cos \theta \cos (\phi_1 - \phi_2) \quad (A6)$$

2. PHYSICAL RELATIONS

Solar divergence:

$$\bar{H}^* = \bar{H}_0^* (R_0/R)^2 \quad (A7)$$

Solar flux equation:

$$\bar{H}^* \cos \xi = \bar{H}_g + \bar{A} + Fc^* \quad (A8)$$

Direct radiation:

$$\bar{H}_{gd} = \bar{H}^* a^{-\sec \xi} = \bar{H}^* \exp (-\tau \sec \xi) \quad (A9)$$

Satellite radiance equation for clouds:

$$\bar{N}/\bar{N}_0 \cos \xi = \beta \bar{F}^*/(\bar{H}^* \cos \xi \chi) \quad (A10)$$

Satellite radiance from GOES "count":

$$\bar{N}/\bar{N}_0 = (C/C_0)^2 \quad (A11)$$

Cloud reflectivity:

$$\bar{r} = \bar{F}^*/(\bar{H}^* \cos \xi) \quad (A12)$$

3. APPROXIMATIONS APPROPRIATE TO SOLAR GEOMETRY CALCULATIONS

Hour angle:

$$h \cong \Lambda + \pi - G(\text{hours}) \times \frac{\pi}{12} \quad (A13)$$

Declination:

$$\delta = 0.408 \sin [(d - 81) \times 2\pi/365] \quad (A14)$$

Solar distance ratio:

$$R_0/R \cong 1 + 0.167 \cos [(d - 14) \times 2\pi/365] \quad (A15)$$

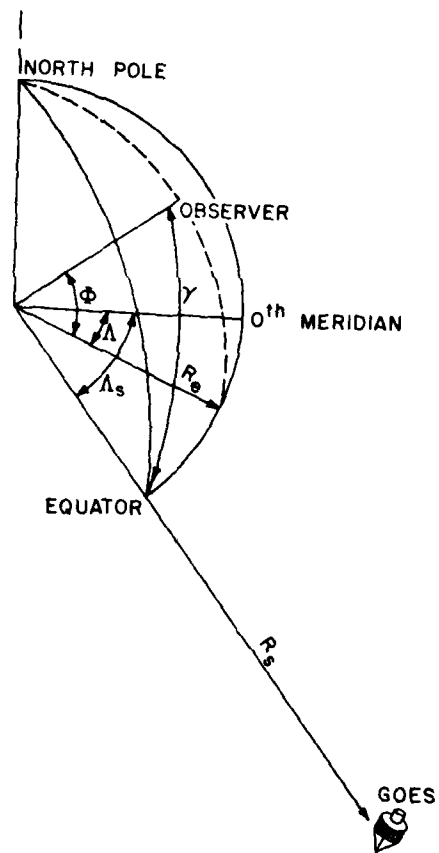


Figure A1. Illustration of Parameters Describing Position of Satellite Relative to Position on Earth

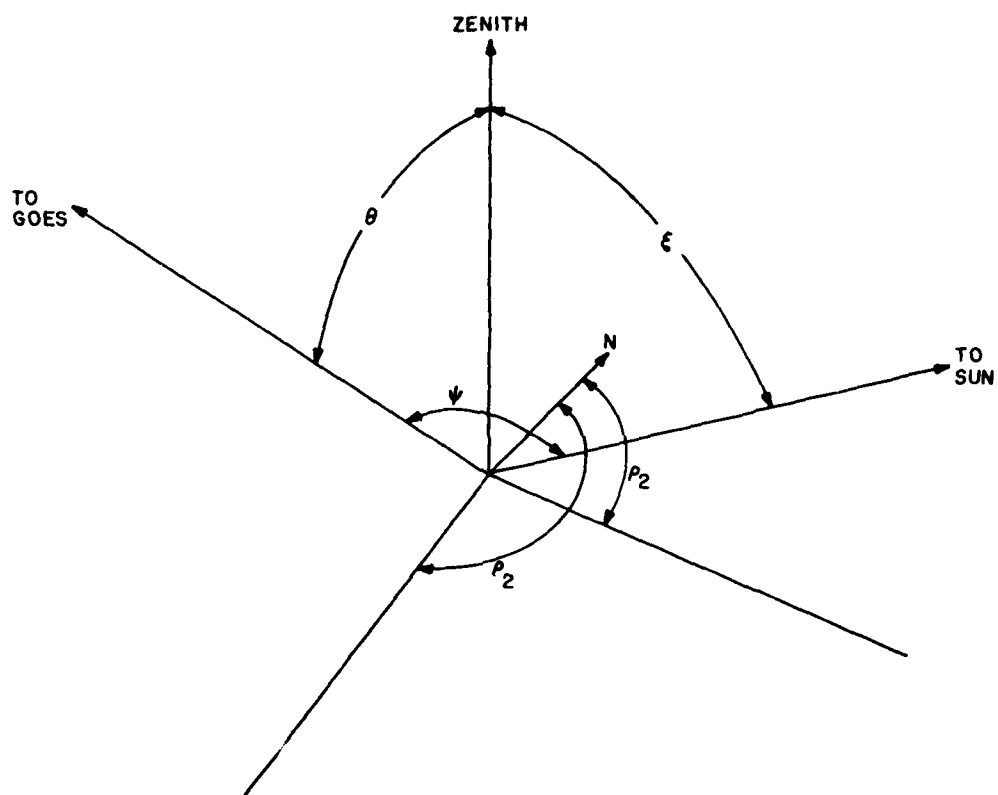


Figure A2. Illustration of Angles Describing Direction of Sun and Direction of Satellite Relative to Position on Earth

Appendix B

Algorithm for Normalizing GOES Video Values[†]

$$\tilde{r} = \left(\frac{C}{C_0} \right)^2 * \sec \xi \quad (B1)$$

$$\Delta\Lambda = |\Lambda_2 - \Lambda_1| \quad (B2)$$

$$C_1 = \cos ((\xi - 50) * 1.8)^2$$

$$C_2 = 0.7 * \cos ((\xi - 22.5) * 4) * (1 + \cos \xi) \quad (B3)$$

$$C_3 = \cos ((\Delta\Lambda - 70) * 1.3)^8 \quad (B4)$$

$$\chi \cong 1.0 + 0.5 * (1 + \cos (2 * \xi)) + 0.20 (C_1 + C_2) * C_3 \quad (B5)$$

$$\tilde{r}_n = 2 * (1.09 - 1.09 - \tilde{r} * \chi * \left(\frac{R_0}{R} \right)^2) / ((1 + (\cos \xi) 1/2) * \left(\frac{R_0}{R} \right)^2)$$

An example of \tilde{r}_n as a function of GMT and GOES count is shown in Figure B1.

[†]Angles in degrees.

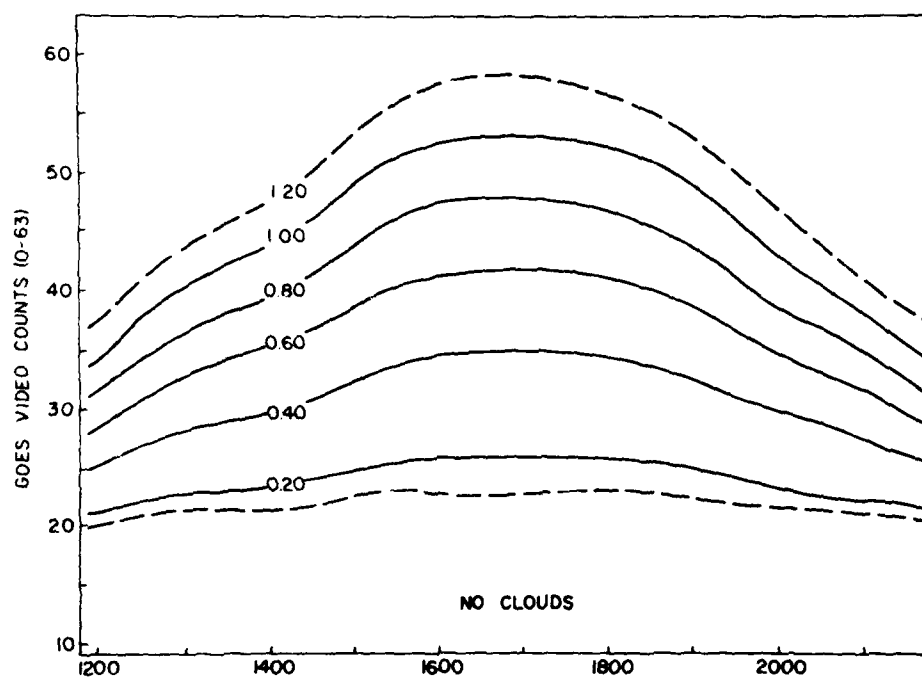


Figure B1. Normalized Cloud Reflectivity as a Function of Video Count and Time of Day, for 16 Apr, 42N and 74W, with Calibration Count (C_0) Equal to 60